Pressure Buildup During Supercritical Carbon Dioxide Injection From a Partially Penetrating Borehole Into Gas Reservoirs

Sumit Mukhopadhyay[1], Shao-Yang Yang[2], and Hund-Der Yeh[3]

Abstract

Injecting CO_2 into a subsurface formation causes a buildup of pressure in the vicinity of the injection well. While a large injection rate can reduce the cost associated with injection, an indefinitely large injection rate can result in excessive formation damage. To obtain an optimal injection rate without exceeding the safe pressure limits, one will like to have some knowledge of the transient pressure buildup characteristics resulting from a particular injection rate. While elaborate numerical simulations can provide reliable pressure buildup predictions, they require extensive knowledge about the formation, which is normally not available at the start of an injection process. To alleviate this problem, using some simplifying assumptions, we have developed a solution to predict the transient buildup of pressure resulting from injection of supercritical carbon dioxide from a partially penetrating well into a gas reservoir. The solution in space and time is first obtained in the Fourier-Laplace transform space, and then inverted back into real space (in cylindrical coordinates) and time. We use the solution to study pressure transient characteristics for different formation permeabilities and anisotropy ratios. Results obtained using the solution compared well with those from numerical simulations.

Keywords: carbon dioxide; storage; sequestration; pressure buildup; supercritical; analytical solution; gas reservoir

1. Introduction

Capturing carbon dioxide from flue gases and injecting them into deep subsurface formations, a process commonly known as geologic storage, has been receiving increasing attention as a viable option for mitigating atmospheric emissions and reversing the global trends of rising surface temperatures (IPCC, 2005). Geologic storage aims to prevent CO_2 from entering the atmosphere by storing it permanently in three main subsurface formations – deep saline aquifers, unminable coal beds, and depleted natural gas reservoirs (Gunter et al., 1996; Bachu, 2000; Gale, 2004; IPCC, 2005; Hepple and Benson, 2005; Holloway, 2005; Oldenburg, 2006; Bachu, 2008; Birkholzer and Zhou, 2009, Vilarrasa et al., 2010a). Of these three main subsurface formations, natural gas

[1] Earth Sciences Division, Lawrence Berkeley National Laboratory, Berkeley, CA, USA
[2] Department of Civil Engineering, Vanung University, Chungli, Taiwan
[3] Institute of Environmental Engineering, National Chiao Tung University, Hsinchu, Taiwan

reservoirs currently appear to be quite appealing (see Ferronato et al., 2010 and references therein).

Injection of CO_2 into deep geological formations is achieved by pumping it down into an injection well. While the actual geological storage zone can be quite thick (ranging from a few meters to tens of meters), only a small part of the injection well (typically, a few meters to 10 or 20 meters) within the storage zone is perforated to allow the injected CO_2 to enter the storage zone. The thickness of the perforated zone depends on the permeability and thickness of the formation. Injection raises the pressure in the immediate vicinity of the well, enabling CO_2 to enter the pore spaces initially occupied by the formation fluids. The spatial and temporal distribution of pressure buildup in the formation will obviously depend on the rate of injection, the permeability, porosity, and thickness of the storage formation, the perforation thickness, and other geological features (such as presence of faults or permeability barriers) of the storage formation.

In this paper, we offer a solution to predict the pressure buildup resulting from injection of CO_2 into a natural gas reservoir where the injection well is partially perforated. Over the years, a large number of analytical and semi-analytical solutions have been developed for flow of gases through porous and permeable formations, a comprehensive review of which is beyond the scope of this paper. To the best of our knowledge, the governing equations for pressure-driven isothermal flow of gases in porous media, assuming ideal gas behavior, were first developed by Leibenzon (1929), and later by Muskat (1946). Later, Al-Hussainy et al. (1966) investigated the flow of real gases (i.e., gases that do not follow the ideal gas law) through porous media using the concept of a pseudo gas pressure. The pseudo pressure concept (Al-Hussainy et al., 1966) has since become a useful tool in studies of gas reservoir engineering. The mass balance equation in Al-Hussainy et al. (1966, equation 18) is non-linear and rigorously valid for arbitrary pressure gradients. It also recognizes the pressure-dependence of viscosity (μ) and compressibility (c_g) of real gases, even though they linearize the governing equations by imposing the assumption that μc_g is constant. For constant rate of production from a gas

reservoir, Al-Hussainy et al. (1966) postulated that evaluating the product μc_g at initial reservoir pressure provided reasonable engineering results. For gas injection problems, it has been noted that evaluating μc_g about half way between the extremes might be quite good (Al-Hussainy et al., 1966; Tartakovsky, 2000).

More recently and with immediate relevance to subsurface injection of CO_2, Saripalli and McGrail (2002) developed semi-analytical solutions for modeling deep well injection of CO_2 into brine formations. As observed latter by Mathias et al. (2009a,b), a limitation of these semi-analytical solutions is that they are developed assuming that both the geological formations and the fluids are incompressible. Subsequently, Mathias et al. (2009a) developed an approximate similarity solution, which describes the spatial and temporal distribution of pressure resulting from CO_2 injection in brine aquifers, and these pressure buildup results were latter used (Mathias et al., 2009b) for assisting in selection of CO_2 sequestration sites. Zhou and Birkholzer (2011) analyzed the magnitude of pressure perturbation and brine migration induced by geologic carbon sequestration assuming a full-scale deployment scenario in which enough CO_2 was captured and stored to make relevant contributions to global climate change mitigation. Analytical solutions have also been obtained for estimating risks of pressure buildup resulting from CO_2 injection (see Oruganti et al., 2011) and for pressure buildup in overlying formations (Zeidouni et al., 2011). Further, Mathias et al. (2011) presented an explicit approximate solution for estimating pressure buildup due to injection of CO2 into closed brine aquifers of finite radial extent.

Note that the analytical or semi-analytical solutions described above pertain to pressure buildup resulting from CO_2 injection in a brine aquifer. The focus of this paper, on the other hand, is on pressure buildup in a gas reservoir. Additionally, some of these previous works (Zhou et al., 2009; Mathias et al., 2009a,b) have assumed that the gas compressibility is constant and independent of pressure. As has been noted earlier (e.g., Al-Hussainy et al., 1966), compressibility of gases, whether behaving ideally or otherwise, is a function of pressure. In some of those works (Mathias et al., 2009a,b), it has been further assumed that the gas compressibility is comparable to the

compressibility of water. As has been noted by Vilarrasa et al. (2010b), CO_2 compressibility is one to two orders magnitude larger than that of the rock or water. They (Vilarrasa et al., 2010b) therefore investigate the impact of CO_2 compressibility on CO_2 storage. They propose a method to account for compressibility effects and viscosity variations, and apply it to the analytical solutions of Nordbotten et al. (2005) and Dentz and Tartakovsky (2009). They, however, do so without actually specifying a relationship (such as an equation of state) between density (or, compressibility) and pressure. Instead, they iteratively solve a non-linear integral equation to obtain the mean density within a plume volume.

In this paper, we show that a solution can be obtained through specification of a suitable equation of state. Moreover, our conceptual model accounts for the partial penetration of the injection well. The effect of partial penetration of the injection well has been studied in the groundwater literature (e.g., Dougherty and Babu, 1984; Hyder at al., 1994; Yang et al., 2006; Yeh et al., 2008). However, to the best of our knowledge, it has not been included in a solution in the context of CO_2 injection and subsurface sequestration. Finally, the solution (for head distribution in a groundwater aquifer containing a partially penetrating well) provided by Dougherty and Babu (1984), is in Laplace-domain. Dougherty and Babu (1984) used a numerical inversion scheme to obtain the solution in real time. By adopting the approach developed by Yeh et al. (2003) and Yang et al. (2006) in this paper, we avoid the errors that might be introduced by the numerical inversion scheme.

One major difficulty in developing an analytical or semi-analytical solution involving injection of CO_2 is that under most formation conditions it behaves as a supercritical fluid, which has a density similar to that of a liquid, while its viscosity is similar to that of a gas. It has been generally concluded (Garcia, 2003; Pruess, 2005) that Altunin's correlations (Altunin, 1975) provide reasonably accurate estimates of CO_2 physical properties. However, these correlations have complex functional forms making them difficult to use for our purposes. We thus propose to use the Pitzer's correlations, after introducing some correction terms to make them consistent with Altunin's correlations.

The rest of the paper is organized as follows. In section 2, we describe the conceptual model for migration of CO_2 after being injected into the formation. In Section 3, we discuss the Pitzer's correlations for computing the physical properties of carbon dioxide, compare the Pitzer's correlations with Altunin's correlations, and introduce corrections terms to the Pitzer's correlations so that their predictions are more consistent with Altunin's correlations. In Section 4, we develop the governing equations along with the initial and boundary conditions specifying the CO_2 injection problem. The solution procedure in Fourier and Laplace transform space is outlined in Section 5. Section 5 also discusses the inversion of the Fourier and Laplace transform space solution to real time. In Section 6, we present the details of the numerical simulations, which were used to verify the solutions. Section 7 discusses the results for some typical injection scenarios and parametric studies involving different formation parameters, which are followed by a summary of the paper in Section 8.

2. Conceptual Model

When CO_2 is injected into the storage formation, different transport mechanisms control its migration thereafter. Depending upon the nature of the fluids already residing in the formation, these transport mechanisms may include fluid flow under pressure gradient created by the injection process, buoyancy caused by density difference between the injected and formation fluids, diffusion, dispersion and fingering (arising from formation heterogeneities and mobility contrast between the fluids), capillarity (resulting from different wetting characteristics of the fluids concerned), dissolution into the formation fluid, mineralization, and adsorption of CO_2 (IPCC, 2005).

For developing an explicit solution, some simplifying assumptions are needed such that the processes that have minor affects or are not important can be excluded from the conceptual model. For example, we exclude processes such as mineralization and adsorption because these processes occur over a long temporal scale, whereas our primary objective is to obtain pressure buildup during or immediately after injection. We also exclude dispersion processes by considering a homogeneous (even though

anisotropic) formation. This is again justified because dispersion seems to play an important role only over large times.

The buoyancy forces that drive vertical flow depend on the type of the fluid in the formation. When CO_2 is injected into a natural gas reservoir, the magnitude of the density difference between the injected gas and the in-situ gas phase depends on formation pressure and temperature, which may lead to significant buoyancy forces. However, note that our objective is to estimate pressure buildup near an injection well, which is dominated by viscous forces and not buoyancy forces (which are important farther away). Consequently, we exclude buoyancy from our conceptual model. This exclusion is likely to produce a conservative estimate of the maximum extent of pressure buildup. This is because buoyancy drives fluids away vertically from the point of injection into the formation. Thus, the predicted pressure without buoyancy at the point of injection is larger than the actual pressure (when buoyancy is included). Additionally, when buoyancy is ignored, the model results provide the maximum limit of horizontal migration of the injected CO_2 (i.e., the actual horizontal spreading may be less when buoyancy is included). Even though the viscosity of pure CO_2 can be significantly larger than that of pure CH_4 (Oldenburg and Doughty, 2010), for the sake of consistency, we assume that the viscosity of the resident gas phase is similar to that of the injected gas.

Figure 1 schematically (not to scale) shows the essential elements of the conceptual model. The storage formation is conceptualized as an infinite circular cylinder ($R_\infty \to \infty$) which has a thickness of L. The origin of the coordinate system is located at the centre in the bottom plane of the circular cylinder, as shown in Figure 1. CO_2 is injected through an injection borehole with radius r_w, which extends all the way to the ground surface. Note that the flow and transport processes inside the injection borehole are not explicitly modeled. As shown in Figure 1, the injection borehole is perforated between b_1 (the height of the bottom of perforated zone from the origin) and b_2 (the height of the top of the perforated zone from the origin). The thickness of the perforated zone thus is $(b_2 - b_1)$, which is considerably smaller than the thickness of the storage formation, L. It

is assumed that CO_2 enters the formation through the perforated zone at a mass flow rate of $\dot{m}$ (in units of kg s^{-1}) for a specified period of time, t_{inj}.

It is assumed that the storage formation is overlain and underlain by thick impervious rocks. In other words, no flow boundary conditions are applied at the top and bottom boundaries of the storage formation. At the radial boundaries (which are assumed to be located at a large distance from the injection borehole), constant pressure $(P = P_i)$ is assumed. It is also assumed that the entire injection process happens under isothermal conditions. Because the average geothermal gradient in most cases is about 25°C per kilometer (IPCC, 2005), for a storage formation, which is about 100 m thick, the temperature difference between the top and bottom of the formation is of the order of 2.5°C. Thus, assuming an isothermal operation is justified. Because we assume isothermal conditions, all thermal effects including Joule-Thompson effects (Oldenburg, 2007) are ignored. It is also assumed that the storage formation was initially (i.e., before injection commenced) maintained at a uniform pressure of P_i. Recognizing that most subsurface formations exhibit anisotropy in their permeabilites, it is assumed that the storage formation has a horizontal permeability of k_r and a vertical permeability of k_z, with an anisotropy ratio of $\alpha = k_z / k_r$. Finally, because we are focusing on injecting CO_2 into a natural gas reservoir, capillarity is not included in the model.

3. Physical Properties of Carbon Dioxide

We begin with the generalized Pitzer correlations (Smith and Van Ness, 1981) for computing the physical properties of CO_2. The generalized Pitzer correlations are based on the virial equation of state (EOS), i.e.,

$$Z \equiv \frac{PV}{RT} = 1 + B'P + C'P^2 + D'P^3 \cdots . \quad (1)$$

In Equation 1, V is volume, T is temperature, R is the universal gas constant, and B', C', D', etc., are the virial coefficients. The simplest correlation proposed by Pitzer is for the

second virial coefficient (B'). It is based on Equation 1 (when truncated after the second term) and can be expressed as

$$Z = 1 + \frac{BP}{RT} \tag{2}$$

where we have used the notation $B' = \frac{B}{RT}$. The range of P and T over which the above generalized correlations can be used can be obtained from the condition

$$V_r \equiv \frac{V}{V_c} \geq 2 . \tag{3}$$

where V_c is the critical volume of carbon dioxide.

The relative simplicity of the generalized Pitzer's correlations does much to use them. However, we need to first test whether these correlations are useful for determining properties of supercritical CO_2, and if so, how they compare against other EOSs such as the Altunin's correlations. To check the range over which Pitzer's correlations can be used for CO_2, we show V_r as a function of P at three different temperatures (31.04°C, which is the critical temperature of CO_2, 55.04°C, and 75.04°C) in Figure 2. Note that the values of the reduced volume were obtained from the CO2TAB file distributed with the TOUGH2/ECO2N software (Pruess, 2005). Note also that the reduced volumes in TOUGH2/ECO2N are calculated using Altunin's correlations. The horizontal dashed line in Figure 2 represents $V_r = 2$. From Figure 2, we observe that, when T = 31.04°C, Pitzer's correlations can be used all the way up to the critical pressure (72.8 atm), beyond which V_r becomes smaller than 2.0. However, as the temperature is increased, Pitzer's correlations can be used even beyond the critical pressure. For example, when temperature is 75.04°C, Pitzer's correlations can be used up to a pressure of 100 atm without any correction terms.

Next, we compare the densities calculated by Altunin's correlations with those from the generalized Pitzer's correlations. Figure 3a shows the difference between the density calculated using Altunin's correlations (ρ) and that obtained from generalized Pitzer's correlations (ρ_P) as a function of pressure at different temperatures (T = 45°C, 55°C,

65°C, 75°C, and 85°C). Because we are interested only in supercritical CO_2, the plots are shown only for temperatures larger than the critical temperature (31.04°C). We can make a number of observations from Figure 3a. First, densities predicted by generalized Pitzer's correlations are always smaller compared to those predicted by Altunin's correlations (i.e., Pitzer's correlations underpredict CO_2 densities). Second, at pressures smaller than the critical pressure (72.8 atm), the difference between the two is small irrespective of temperature. Third, the difference between Altunin's predictions and Pitzer's correlations (with respect to density) decreases with increasing temperature. Finally, note that the difference in densities predicted by the Altunin's and Pitzer's correlations initially increases with increase in pressure, passes through a peak, and then decreases thereafter. We may call the pressure at which the density difference reaches a peak as the turnover pressure, P_{to}, which is different at different temperatures.

It is our hypothesis that, if suitable correction terms are used, the Pitzer's correlations can be extended to obtain density values at pressures as large as P_{to}. In other words, we propose a relationship of the form

$$\rho - \rho_P = \sum_{n=0}^{3} a_n P^n, P \le P_{to} \tag{4}$$

where ρ is the density of supercritical CO_2 predicted by Altunin's correlations, ρ_P is the same predicted by Pitzer's correlations, P is pressure, and the coefficients (a_n) are functions of temperature. The values of the coefficients a_n at different temperatures are given in Table 1, which also provides the range of pressure over which Equation 4 can be used. For sake of completeness, we show the actual and fitted density differences at different temperatures in Figure 3b.

4. Governing Equations and Boundary Conditions

The balance equation for flow of carbon dioxide under isothermal conditions can be described as

$$\Delta t\left[2\pi r\Delta z q_r \rho\big|_r - 2\pi r\Delta z q_r \rho\big|_{r+\Delta r} + 2\pi r\Delta r q_z \rho\big|_z - 2\pi r\Delta r q_z \rho\big|_{z+\Delta z}\right] = 2\pi r\Delta r\Delta z\phi\rho\big|_{t+\Delta t} - 2\pi r\Delta r\Delta z\phi\rho\big|_t \quad (5)$$

At the limit $\Delta r, \Delta z, \Delta t \to 0$, Equation 5 can be written as

$$-\frac{1}{r}\frac{\partial}{\partial r}(rq_r\rho) - \frac{\partial}{\partial z}(q_z\rho) = \phi\frac{\partial\rho}{\partial t}. \quad (6)$$

Assuming Darcy flow regime, we can write $q_r = -\frac{k_r}{\mu}\frac{\partial P}{\partial r}$, and $q_z = -\frac{k_z}{\mu}\frac{\partial P}{\partial z}$. Introducing q_r and q_z in Equation 6, we obtain

$$\frac{1}{r}\frac{\partial}{\partial r}\left(r\rho\frac{\partial P}{\partial r}\right) + \alpha\frac{\partial}{\partial z}\left(\rho\frac{\partial P}{\partial z}\right) = \frac{\phi\bar{\mu}}{k_r}\frac{\partial\rho}{\partial t} \quad (7)$$

where $\alpha = \frac{k_z}{k_r}$ is the ratio of the vertical and horizontal permeabilities (hereafter referred to as anisotropy ratio). In writing Equation 7, we have assumed that the viscosity of carbon dioxide is constant over the pressure range typically encountered during injection in a gas reservoir.

In Equations 5 through 7, $\rho(P,T)$ is the true density of CO_2 (as obtained from, say, Altunin's correlations), which is different from $\rho_P(P,T)$ — the Pitzer density (see Equation 4). By definition

$$\rho_P = \frac{PM}{ZRT} \quad (8)$$

where *M* is the molecular weight of carbon dioxide (0.044 kg/mol). Eliminating Z between Equations 2 and 8, we obtain an expression relating *P* to ρ_P

$$P = \frac{\rho_P RT}{M - B\rho_P}. \quad (9)$$

Combining Equations 4 and 9, we obtain the relationship

$$\rho = \rho_P + \sum_{n=0}^{3} a_n\left(\frac{\rho_P RT}{M - B\rho_P}\right)^n. \quad (10)$$

Introducing Equation 10 into Equation 7, we get

$$\frac{1}{r}\frac{\partial}{\partial r}\left(r\left\{\rho_P+\sum_{n=0}^{3}a_n\left(\frac{\rho_P RT}{M-B\rho_P}\right)^n\right\}\frac{\partial P}{\partial r}\right)+\alpha\frac{\partial}{\partial z}\left(\left\{\rho_P+\sum_{n=0}^{3}a_n\left(\frac{\rho_P RT}{M-B\rho_P}\right)^n\right\}\frac{\partial P}{\partial z}\right) = \frac{\phi\bar{\mu}}{k_r}\frac{\partial}{\partial t}\left(\rho_P+\sum_{n=0}^{3}a_n\left(\frac{\rho_P RT}{M-B\rho_P}\right)^n\right) \quad (11)$$

After changing the differentials $\frac{\partial P}{\partial r}$ and $\frac{\partial P}{\partial z}$ to $\frac{\partial \rho_P}{\partial r}$ and $\frac{\partial \rho_P}{\partial z}$, respectively, we can write Equation 11 as

$$\frac{1}{r}\frac{\partial}{\partial r}\left(\frac{r}{(M-B\rho_P)^2}\left\{\rho_P+\sum_{n=0}^{3}a_n\left(\frac{\rho_P RT}{M-B\rho_P}\right)^n\right\}\frac{\partial \rho_P}{\partial r}\right)+\alpha\frac{\partial}{\partial z}\left(\frac{1}{(M-B\rho_P)^2}\left\{\rho_P+\sum_{n=0}^{3}a_n\left(\frac{\rho_P RT}{M-B\rho_P}\right)^n\right\}\frac{\partial \rho_P}{\partial z}\right)= \frac{\phi\bar{\mu}}{MRTk_r}\frac{\partial}{\partial t}\left(\rho_P+\sum_{n=0}^{3}a_n\left(\frac{\rho_P RT}{M-B\rho_P}\right)^n\right) \quad (12)$$

To simplify Equation 12, we introduce a new variable, $\psi = M - B\rho_P$, which transforms Equation 12 into

$$\frac{1}{r}\frac{\partial}{\partial r}\left(r\left\{\frac{M-\psi}{\psi^2}+\frac{a_0 B}{\psi^2}+\sum_{n=1}^{3}\frac{a_n R^n T^n}{B^{n-1}\psi^2}\left(\frac{M-\psi}{\psi}\right)^n\right\}\frac{\partial \psi}{\partial r}\right)+$$

$$\alpha\frac{\partial}{\partial z}\left(\left\{\frac{M-\psi}{\psi^2}+\frac{a_0 B}{\psi^2}+\sum_{n=1}^{3}\frac{a_n R^n T^n}{B^{n-1}\psi^2}\left(\frac{M-\psi}{\psi}\right)^n\right\}\frac{\partial \psi}{\partial z}\right)=-\frac{\phi\bar{\mu}B}{MRTk_r}\frac{\partial}{\partial t}\left[(M-\psi)+a_0 B+\sum_{n=1}^{3}\frac{a_n R^n T^n}{B^{n-1}}\left(\frac{M-\psi}{\psi}\right)^n\right] \quad (13)$$

Equation 13 can be further simplified if we define

$$\theta=-\left[\frac{M}{\psi}+\ln\psi+\sum_{n=1}^{4}\frac{d_n}{\psi^n}\right] \quad (14a)$$

where we have defined

$$d_1 = a_0 B - a_1 RT + \frac{a_2 R^2 T^2}{B} - \frac{a_3 R^3 T^3}{B^2} \quad (14b)$$

$$d_2 = M\left(\frac{a_1 RT}{2}-\frac{a_2 R^2 T^2}{B}+\frac{3}{2}\frac{a_3 R^3 T^3}{B^2}\right) \quad (14c)$$

$$d_3 = M^2\left(\frac{1}{3}\frac{a_2R^2T^2}{B} - \frac{a_3R^3T^3}{B^2}\right) \tag{14d}$$

$$d_4 = \frac{M^3}{4}\frac{a_3R^3T^3}{B^2} \tag{14e}$$

Using this definition of θ, Equation 13 is finally written as

$$\frac{1}{r}\frac{\partial}{\partial r}\left(r\frac{\partial\theta}{\partial r}\right) + \alpha\frac{\partial}{\partial z}\left(\frac{\partial\theta}{\partial z}\right) = \frac{1}{\beta}\frac{\partial\theta}{\partial t} \tag{15}$$

where β (which has units of diffusivity, m^2/s) is defined as

$$\beta = \frac{k_r MRT}{\phi\bar{\mu}B}\left[\frac{\frac{M-\bar{\psi}}{\bar{\psi}^2} + \frac{a_0B}{\bar{\psi}^2} + \frac{a_1RT}{\bar{\psi}^3}\left(M-\bar{\psi}\right) + \frac{a_2R^2T^2}{B}\frac{\left(M-\bar{\psi}\right)^2}{\bar{\psi}^4} + \frac{a_3R^3T^3}{B^2}\frac{\left(M-\bar{\psi}\right)^3}{\bar{\psi}^5}}{1 + \frac{Ma_1RT}{\bar{\psi}^2} + \frac{2Ma_2R^2T^2}{B}\frac{\left(M-\bar{\psi}\right)}{\bar{\psi}^3} + \frac{3Ma_3R^3T^3}{B^2}\frac{\left(M-\bar{\psi}\right)^2}{\bar{\psi}^4}}\right] \tag{16}$$

Note that equation 15 is obtained by linearization of Equation 13. Al-Hussainy et al. (1966) used a similar linearization procedure while developing their gas flow equations in terms of the pseudo-reduced pressure (see Section 1 for more discussion on this). In addition, one can write the compressibility factor of CO_2

$$\frac{1}{c_g} = \frac{MRT}{B}\left[\frac{\frac{M-\bar{\psi}}{\bar{\psi}^2} + \frac{a_0B}{\bar{\psi}^2} + \frac{a_1RT}{\bar{\psi}^3}\left(M-\bar{\psi}\right) + \frac{a_2R^2T^2}{B}\frac{\left(M-\bar{\psi}\right)^2}{\bar{\psi}^4} + \frac{a_3R^3T^3}{B^2}\frac{\left(M-\bar{\psi}\right)^3}{\bar{\psi}^5}}{1 + \frac{Ma_1RT}{\bar{\psi}^2} + \frac{2Ma_2R^2T^2}{B}\frac{\left(M-\bar{\psi}\right)}{\bar{\psi}^3} + \frac{3Ma_3R^3T^3}{B^2}\frac{\left(M-\bar{\psi}\right)^2}{\bar{\psi}^4}}\right] \tag{17a}$$

An alternative expression for compressibility factor can also be obtained (in terms of pressure and temperature), which is

$$c_g = \frac{\frac{MRT}{\left(BP+RT\right)^2} + \sum_{n=1}^{3} na_nP^{n-1}}{\frac{PM}{BP+RT} + \sum_{n=0}^{3} a_nP^n}. \tag{17b}$$

We now need to develop an expression for θ as a function of either pressure or density. Observe that

$$\psi = M - B\rho_P = M - B \times \frac{M}{BZ}(Z-1) = \frac{M}{Z}. \tag{18}$$

Combining the definition of θ with Equation 18, we have

$$\theta = -\left[Z + \ln\frac{M}{Z} + \sum_{n=1}^{4} d_n \left(\frac{Z}{M}\right)^n \right]. \tag{19}$$

It is now easy to see that

$$Ze^{-\left(C_1 Z + C_2 Z^2 + C_3 Z^3 + C_4 Z^4\right)} = Me^{\theta} \tag{20}$$

where $C_1 = 1 + \frac{d_1}{M}$, $C_2 = \frac{d_2}{M^2}$, $C_3 = \frac{d_3}{M^3}$, and $C_4 = \frac{d_4}{M^4}$. Thus, once θ is known from Equation 15, Z can be obtained by solving Equation 20. $P(r,z,t)$ can then be obtained from

$$P(r,z,t) = \frac{RT}{B}\left[Z(r,z,t) - 1\right] \tag{21}$$

The initial and boundary conditions for pressure are

$$P(r,z,0) = P_i \ , \tag{22a}$$

$$\frac{\partial P}{\partial z}\Big|_{z=0} = 0 \ , \tag{22b}$$

$$\frac{\partial P}{\partial z}\Big|_{z=L} = 0 , \tag{22c}$$

$$P(\infty,z,t) = P_i , \tag{22d}$$

and

$$2\pi r_w (b_2 - b_1)\frac{k_r}{\mu}\rho \frac{\partial P}{\partial r}\Big|_{r=r_w} = \dot{m}\left[U(z-b_1) - U(z-b_2)\right]. \tag{22e}$$

where $U(z-\chi)$ is defined as the unit step function such that

$$U(z-\chi)=0, z<\chi \\ =1, z\geq\chi \tag{22f}$$

In other words, this translates to non-zero carbon dioxide injection into the storage formation through the perforated zone, and zero injection of the same through other parts of the injection well.

For the transformed compressible factor, $\theta(r,z,t)$, the initial and boundary conditions become

$$\theta(r,z,0)=\theta_i, \tag{23a}$$

$$\frac{\partial\theta}{\partial z}\Big|_{z=0}=0, \tag{23b}$$

$$\frac{\partial\theta}{\partial z}\Big|_{z=L}=0, \tag{23c}$$

$$\theta(\infty,z,t)=\theta_i, \tag{23d}$$

and

$$-\frac{\partial\theta}{\partial r}\Big|_{r=r_w}=\frac{\dot{m}\mu B^2}{2\pi r_w(b_2-b_1)k_r MRT}\left[U(z-b_1)-U(z-b_2)\right]. \tag{23e}$$

5. Solution Scheme

Equation 15 is cast into dimensionless form by defining the dimensionless variables $\theta_D=\frac{\theta_i-\theta}{\theta_i}$, $\xi=\frac{r}{r_w}$, $\zeta=\frac{z}{r_w}$, and $\tau=\frac{\beta t}{r_w^2}$, which results in

$$\frac{1}{\xi}\frac{\partial}{\partial\xi}\left(\xi\frac{\partial\theta_D}{\partial\xi}\right)+\alpha\frac{\partial}{\partial\zeta}\left(\frac{\partial\theta_D}{\partial\zeta}\right)=\frac{\partial\theta_D}{\partial\tau} \tag{24}$$

.

The initial and boundary conditions in the dimensionless space are

$$\theta_D(\xi,\zeta,0)=0, \tag{25a}$$

$$\frac{\partial\theta_D}{\partial\zeta}\Big|_{\zeta=0}=0, \tag{25b}$$

$$\left.\frac{\partial \theta_D}{\partial \zeta}\right|_{\zeta=L_D} = 0\,, \tag{25c}$$

$$\theta_D(\infty, \zeta, \tau) = 0\,, \tag{25d}$$

and

$$-\left.\frac{\partial \theta_D}{\partial \xi}\right|_{\xi=1} = \dot{m}_D\left[U(\zeta - B_1) - U(\zeta - B_2)\right]\,. \tag{25e}$$

In Equation 25c, $L_D = \dfrac{L}{r_w}$ is the dimensionless reservoir thickness, and in Equation 25e, $\dot{m}_D = \dfrac{\dot{m}}{2\pi(b_2 - b_1)\dfrac{k_r}{\mu}\theta_i \dfrac{MRT}{B^2}}$, $B_1 = \dfrac{b_1}{r_w}$, and $B_2 = \dfrac{b_2}{r_w}$. $(B_2 - B_1)$ is the dimensionless perforation thickness.

To solve Equation 24, we first define the finite Fourier cosine transform of $\theta_D(\xi, \zeta, \tau)$ as

$$\tilde{\theta}_D(\xi, \omega_n, \tau) = \int_0^{L_D} \theta_D(\xi, \zeta, \tau)\cos(\omega_n \zeta)\, d\zeta \qquad 0 \le \zeta \le L_D \tag{26}$$

where $\omega_n = \dfrac{n\pi}{L_D}$. In the Fourier cosine transform space, Equation 24 can be rewritten as

$$\frac{1}{\xi}\frac{\partial}{\partial \xi}\left(\xi \frac{\partial \tilde{\theta}_D}{\partial \xi}\right) - \alpha \omega_n^2 \tilde{\theta}_D = \frac{\partial \tilde{\theta}_D}{\partial \tau}\,. \tag{27}$$

Note that in developing Equation 27, we have used the property

$$F\left[\frac{\partial^2 \theta_D}{\partial \zeta^2}\right] = (-1)^n \left.\frac{\partial \theta_D}{\partial \zeta}\right|_{\zeta=L_D} - \left.\frac{\partial \theta_D}{\partial \zeta}\right|_{\zeta=0} - \omega_n^2 \tilde{\theta}_D \tag{28}$$

in conjunction with the conditions specified in Equations 25b and 25c. We next define the Laplace transform such that

$$\hat{\tilde{\theta}}_D(\xi, \omega_n, p) = \int_0^{\infty} \tilde{\theta}_D(\xi, \omega_n, \tau) e^{-p\tau}\, d\tau\,. \tag{29}$$

In the Laplace transform space, Equation 28 becomes

$$\frac{1}{\xi}\frac{d}{d\xi}\left(\xi\frac{d\hat{\hat{\theta}}_D}{d\xi}\right)=q_1^2\hat{\hat{\theta}}_D \tag{30}$$

where $q_1=\sqrt{p+\alpha\omega_n^2}$. Note that in writing Equation 30, we have used the initial condition given by Equation 25a. Note also that in the Fourier-Laplace-transform space the boundary condition given in Equation 25e becomes

$$\frac{d\hat{\hat{\theta}}_D}{d\xi}\Big|_{\xi=1}=-\frac{\dot{m}_D}{\omega_n p}\left[\sin(\omega_n B_2)-\sin(\omega_n B_1)\right]. \tag{31}$$

The detailed procedure for obtaining the solution for Equation 31 can be found in Yeh et al. (2003) and Yang et al. (2006). Here we provide the solution without providing the intermediate steps. The solution of Equation 31 can be written as

$$\hat{\hat{\theta}}_D(\xi,\omega_n,p)=\frac{\dot{m}_D\left[\sin(\omega_n B_2)-\sin(\omega_n B_1)\right]}{\omega_n p q_1}\frac{K_0(q_1\xi)}{K_1(q_1)}. \tag{32}$$

Performing an inverse Fourier transform (Yeh et al., 2003; Yang et al., 2006), we obtain the following in the Laplace transform space

$$\hat{\theta}_D(\xi,\zeta,p)=\frac{\dot{m}_D}{p\sqrt{p}}\frac{(B_2-B_1)}{L_D}\frac{K_0\left(\xi\sqrt{p}\right)}{K_1\left(\sqrt{p}\right)}+\frac{2\dot{m}_D}{L_D}\sum_{n=1}^{\infty}\frac{K_0(q_1\xi)}{pq_1K_1(q_1)}\frac{\left[\sin(\omega_n B_2)-\sin(\omega_n B_1)\right]}{\omega_n}\cos(\omega_n\zeta) \tag{33}$$

A solution in real-time space can now be obtained using the procedures elaborated in (see Appendix A). This solution is

$$\theta_D(\xi,\zeta,\tau)=\frac{2\dot{m}_D}{\pi L_D}\left[(B_2-B_1)f_{1D}(\xi,\tau)+2\sum_{n=1}^{\infty}f_{2D}(\xi,\tau)\frac{\sin(\omega_n B_2)-\sin(\omega_n B_1)}{\omega_n}\cos(\omega_n\zeta)\right] \tag{34}$$

where

$$f_{1D}(\xi,\tau)=\int_0^{\infty}\left(1-e^{-u^2\tau}\right)\frac{Y_0(\xi u)J_1(u)-J_0(\xi u)Y_1(u)}{Y_1^2(u)+J_1^2(u)}\frac{du}{u^2}, \tag{35}$$

and

$$f_{2D}(\xi,\tau)=\int_0^{\infty}\left[1-e^{-\left(u^2+\alpha\omega_n^2\right)\tau}\right]\frac{Y_0(\xi u)J_1(u)-J_0(\xi u)Y_1(u)}{Y_1^2(u)+J_1^2(u)}\frac{du}{u^2+\alpha\omega_n^2}. \qquad (36)$$

6. Numerical Simulations

We performed numerical simulations to obtain an estimate of pressure buildup for a specified injection rate and formation properties. Results from these numerical simulations can be useful in validating and verifying the results from our solution scheme. The numerical simulations are carried out using the ECO2N module (Pruess, 2005) of the TOUGH2 numerical simulator (Pruess et al., 1999). ECO2N is a fluid property module for mixtures of water, NaCl, and CO_2, and is specifically developed for use with TOUGH2, which is a general purpose simulator for nonisothermal flows of multicomponent, multiphase fluids in porous and fractured formations. For our purpose, we developed a two-dimensional, radial mesh representing the storage formation. The formation is 100 m thick (in the vertical direction). The wellbore radius is assumed to be 0.1 m and the perforation thickness is assumed to be 10 m. These perforations are located between 45 m and 55 m from the bottom of the formation. Note that the wellbore is not modeled explicitly. The mesh is refined near the wellbore, however, it coarsens farther away from the injection point.

To realize a constant pressure outer boundary, we inserted an element with large volume at a large distance (approximately 10,000 kilometer) from the injection well. The top and bottom boundaries are assumed to be closed boundaries. Because most gas reservoirs are low-pressure formations, often below 1MPa, we assume that the storage formation is initially at 0.5 MPa. We also assume that the formation porosity is 0.1 and permeability is 1×10^{-14} m^2. The imposed injection rate is 250,000 tons/year and it is assumed that injection continues for 30 years. Formation temperature is assumed to be 55^oC. Assuming a geothermal gradient of 0.03^oC, and a surface temperature of 20^oC, a formation temperature of 55^oC corresponds to a formation depth of 1167 m or approximately 3800 ft. The parameters used in the numerical simulations and for obtaining the solutions are summarized in Table 2.

7. Results and Discussion

For the first set of results obtained with the proposed solution scheme, the injection rate, initial and boundary conditions, and the formation properties (thickness, perforation thickness, permeability and porosity) are summarized in Table 2, i.e., they are identical to those used for the numerical simulations. Pressure versus time behavior at three different radial locations (r = 0.1, 1.0, and 10.0 meters) are shown in Figure 4. These locations are selected because they are close to the injection well, and are expected to experience the largest increase in pressure and also the largest pressure gradient. For locations very close to the borehole (r = 0.1 or 1.0 m), pressure increases rapidly over the first few thousands to ten thousand seconds of carbon dioxide injection, Thereafter, pressure changes less rapidly before a steady state is attained. Farther from the borehole (e.g., r = 10.0 m), increase in pressure happens at a slower rate and the maximum rise in pressure is also smaller.

In Figure 4, we also compare the analytical solutions (solid lines) with the numerical simulation results (symbols). The analytical solutions generally compare well with the numerical simulation results, particularly after about 4-6 hours. By the end of the 30 years injection period, both the analytical solutions and the simulation results predict that the maximum pressure is expected to be about 11.5 MPa (starting at 0.5 MPa), which is within the range of applicability of the corrected Pitzer's correlations at 55^{o}C. The good match between the analytical solutions and the simulation results provide confidence in the modeling approach presented in this paper.

The impact of permeability anisotropy on pressure buildup resulting from carbon dioxide injection is illustrated in Figures 5 and 6. Figure 5 shows pressure as a function of radial distance at one year after injection started for different anisotropy ratios ($\alpha = 10^{-2}$, 10^{-1}, 1, 10^{1}, and 10^{2}). Note that Figure 4 was developed for α = 1, i.e., when the formation permeability was isotropic. When α = 0.1, i.e., when the vertical permeability is one-tenth that of the radial (or horizontal) permeability, it becomes relatively more difficult to

move vertically than horizontally. Thus, at any specified time, more of the injected mass of carbon dioxide reaches a fixed radial location when $\alpha = 0.1$ (compared to the situation when $\alpha = 1$). Consequently, the increase in pressure at a fixed radial location at a specified time is more when $\alpha = 0.1$ (compared to the situation when $\alpha = 1$). This trend is expected to be even more pronounced when α is reduced further (see plot for $\alpha = 0.01$ in Figure 5). The converse is true when vertical permeability is more than radial permeability, as illustrated by the plots for $\alpha = 10$ and 100 in Figure 5. When $\alpha >> 1$, because more carbon dioxide flows in the vertical direction relative to the radial direction, pressure buildup along the radial direction is relatively less severe (compared to the isotropic case).

Pressure as a function of time corresponding to different anisotropy ratios is shown in Figure 6. Note that the pressure buildup curves in Figure 6 correspond to a radial location of $r = 10.0$ m. As α is gradually reduced from 100 to 0.01 (i.e., as vertical permeability is reduced by four orders of magnitude keeping the radial permeability constant), it is observed that pressure rises more and more at any specified time and at a fixed radial location. These results can be easily explained following the same arguments provided for explaining Figure 5.

One of the key factors influencing the extent of pressure buildup is the formation permeability. This is illustrated in Figures 7, which shows pressure as a function of radial distance at 1 year (Figure 7a) and 30 years (Figure 7b) for different radial permeabilities ($k_r = 1\times10^{-13}$, 1×10^{-14}, and 1×10^{-15} m^2). The solid lines in Figures 7a and 7b correspond to analytical solutions, while the symbols represent results from numerical simulation. For Figure 7, we assume that the formation is isotropic ($\alpha = 1$). When the formation is highly permeable ($k_r = 1\times10^{-13}$ m^2), the increase in pressure is limited, and the analytical solutions match well with the simulation results. As permeability is reduced by an order of magnitude ($k_r = 1\times10^{-14}$ m^2), significant buildup in pressure happens, particularly close to the injection borehole. The match between the analytical and simulation results is still quite good. However, when permeability is reduced by another order of magnitude ($k_r = 1\times10^{-15}$ m^2), the analytical solution deviates from the simulation results, particularly close

to the injection well. This is because the expected pressure buildup close to the injection well for this case exceeds the range of applicability of the corrected Pitzer's correlations.

Figure 8 shows essentially the same results as Figure 7, except it shows pressure as a function of time at a radial location of r = 10.0 m (Figure 8a) and 0.1 m (Figure 8b) for three different radial permeabilities (k_r = 1×10^{-13}, 1×10^{-14}, and 1×10^{-15} m^2). At r = 10.0 m (Figure 8a), the match between the analytical solutions and simulation results is good, even at smaller permeabilities. On the other hand, at r = 0.1 m (figure 8b), the match between the analytical solution and the simulation results is good when permeabilities are large (k_r = 1×10^{-13} and 1×10^{-14} m^2). At smaller permeabilities (e.g., k_r = 1×10^{-15} m^2), a maximum difference of 18% in predicted pressure buildup exists between our approach and the numerical simulations at r = 0.1 m (where the pressure perturbations are expected to be the maximum). Farther away (as shown in Figure 8a), the difference between the two approaches is smaller.

8. Summary

In this paper, we offer an explicit solution to predict the extent of pressure buildup resulting from CO_2 injection into a gas reservoir. This solution is not formation-specific, and is general in nature. It is also more appropriate than empirical relationships based on oil and gas operations. These analytical solutions are thus useful in providing guidelines, particularly before start of the injection process.

The storage formation is conceptualized as an infinite cylinder, which has a finite thickness. CO_2 is injected through a borehole, which extends all the way to the ground surface. It is assumed that the thickness of the perforated zone is considerably smaller than the thickness of the formation. It is also assumed that CO_2 enters the formation through the perforated zone at a constant flow rate for a specified period of time. No flow boundary conditions are applied at the top and bottom boundaries of the storage

formation, and constant pressure condition is assumed at the radial boundaries. It is assumed that the entire injection process happens under isothermal conditions. It is also assumed that the storage formation was initially maintained at a uniform pressure. Formation permeabilities are assumed to be anisotropic, consistent with most subsurface storage formations. Finally, because we are focusing on injecting CO_2 into gas reservoirs, capillarity is not included in the model. To obtain maximum limits on pressure buildup near the injection well or on the extent of horizontal spreading, we excluded the effects of buoyancy from the conceptual models.

An appropriate equation of state is needed to estimate the physical properties of supercritical carbon dioxide. In this paper, we use Pitzer's correlations, after introducing correction terms to make them consistent with Altunin's correlations, which have been found to provide accurate estimates of CO_2 properties. We investigate the difference between density values predicted by the Pitzer's correlations and Altunin's correlations, and showed that the difference is a function of pressure. We fitted the difference in density as a polynomial function of pressure, and obtained the fitting coefficients at different temperatures.

The differential equation controlling the spread of CO_2 was obtained from mass balance conditions. The solution to the differential equation was first obtained in the Fourier-Laplace space, and then inverted back to real time and space. Typical pressure buildup plots (both as a function of radial distance and time) are obtained for various formation permeabilities, anisotropy rartios, and temperatures. These results were compared against results from numerical simulations using the TOUGH2-ECO2N software, and a good match was observed, providing confidence in the solution procedure developed in this paper.

Appendix A

The convolution theorem (Hildebrand, 1976, p.63) states that

$$L^{-1}\{f(p)g(p)\} = \int_0^\tau F(\tau-\eta)G(\eta)d\eta \qquad \text{(A.1)}$$

Let the Laplace-domain solution of Equation 33 be expressed as

$$\hat{\theta}_D(\xi,\zeta,p)=\frac{\dot{m}_D}{p\sqrt{p}}\frac{(B_2-B_1)}{L_D}\bar{S}_A+\frac{2\dot{m}_D}{L_D}\sum_{n=1}^{\infty}\bar{S}_B\frac{[\sin(\omega_n B_2)-\sin(\omega_n B_1)]}{\omega_n}\cos(\omega_n\zeta) \qquad \text{(A.2)}$$

where $\bar{S}_A = K_0\left(\xi\sqrt{p}\right)/K_1\left(\sqrt{p}\right)$ and $\bar{S}_B = K_0(q_1\xi)/[pq_1K_1(q_1)]$.

The Laplace inversion of $\bar{S}_A$ can be expressed as

$$S_A = L^{-1}\{\bar{S}_A\} = L^{-1}\{f_1(p)\cdot g_1(p)\} \qquad \text{(A.3)}$$

where $f_1(p)$ equals $1/p$ and $g_1(p)$ represents the term in $\bar{S}_A$ except $1/p$. Applying the Bromwich integral with $L^{-1}\{f_1(p)\} = F(\tau) = 1$ yields [*Hildebrand*, 1976, p.624]

$$L^{-1}\{g_1(p)\} = \frac{1}{2\pi i}\int_{\gamma-i\infty}^{\gamma+i\infty} e^{p\tau}g_1(p)dp = 0 \qquad \text{(A.4)}$$

where p is a complex variable, i is an imaginary unit, and γ is a large, real, and positive constant so that all the poles lie to the left of line (γ - $i\infty$,γ + $i\infty$).

A single branch point with no singularity (pole) at p = 0 exists in the integrand of $\bar{S}_A$. The contour of integrand is shown in Figure 9 with a cut of p plane along a negative real axis, where ε is taken sufficiently small to exclude all poles from the circle about the origin. Along the small circle *EF*, the integration around the origin when ε approaches zero is carried out by using the Cauchy integral and the value of integration is equal to zero. The integrals taken along *BCD* and *GHA* tend to zero when *R* approaches infinity. Therefore, $\bar{S}_A$ can be superseded by the sum of integrals along *DE* and *FG*. In other words, (A4) can be written as

$$G_1(\tau) = \lim_{\substack{\varepsilon\to 0\\ R\to\infty}}\frac{-1}{2\pi i}\left[\int_{DE} e^{p\tau}g_1(p)dp + \int_{FG} e^{p\tau}g_1(p)dp\right] \qquad \text{(A.5)}$$

The result of contour integral can then be obtained by following the method of Yeh et al. (2003) and Yang et al. (2006) as

$$G_1(\tau) = \frac{2}{\pi}\int_0^{\infty} e^{-u^2\tau}\frac{Y_0(\xi u)J_1(u) - J_0(\xi u)Y_1(u)}{Y_1^{\,2}(u) + J_1^{\,2}(u)}du \qquad \text{(A.6)}$$

Therefore, the complete solution obtained by the convolution is

$$S_A(\xi,\tau)=\int_0^{\tau}1\cdot G_1(\eta)d\eta \tag{A.7}$$

The result of (A7) after the integration is

$$S_A=\frac{2}{\pi}\int_0^{\infty}(1-e^{-u^2\tau})\frac{Y_0(\xi u)J_1(u)-J_0(\xi u)Y_1(u)}{Y_1^{\,2}(u)+J_1^{\,2}(u)}\frac{du}{u^2} \tag{A.8}$$

The first shifting theorem of the Laplace transforms states

$$L^{-1}\{p-a\}=e^{a\tau}L^{-1}\{p\} \tag{A.9}$$

Based on $\bar{S}_B(p)=f_1(p)g_1(p+\alpha\omega_n^{\,2})$, the Laplace inversion of $\bar{S}_B(p)$ is

$$S_B(\xi,\tau)=\int_0^{\tau}1\cdot e^{-\alpha\omega_n^{\,2}\eta}G_1(\eta)d\eta \tag{A.10}$$

Thus, the result of (A.10) after the integration is

$$S_B=\frac{2}{\pi}\int_0^{\infty}(1-e^{-(u^2+\alpha\omega_n^{\,2})\tau})\frac{1}{(u^2+\alpha\omega_n^2)}\frac{Y_0(\xi u)J_1(u)-J_0(\xi u)Y_1(u)}{Y_1^{\,2}(u)+J_1^{\,2}(u)}du \tag{A.11}$$

Combining (A.8) and (A.11), one can then obtain the time-domain solution of Equation 34 in the text.

Nomenclature

B	$= B'RT$ (see below), m^3/mol
B', C', D'…	virial coefficients (see Equation 1)
b_1	height of the bottom of the perforated zone, m
b_2	height of the top of the perforated zone, m
k_r	permeability in the radial direction, m^2
k_z	permeability in the vertical direction, m^2
L	thickness of the storage formation
P	pressure, atm
P_c	critical pressure, atm
P_i	initial pressure and pressure at an infinitely large radial distance, atm
P_r	reduced pressure
q_r	volume flux of CO_2 in the radial direction, m s^{-1}
q_z	volume flux of CO_2 in the vertical direction, m s^{-1}
R	universal gas constant, J mol^{-1} K^{-1}
r	radial coordinate or radial distance from the centre of the injection borehole, m
Δr	infinitesimal radial distance, m
T	temperature, K
T_c	critical temperature, K
T_r	reduced temperature

t	time, s
V_r	reduced volume
Z	compressibility factor.
z	vertical coordinate or vertical distance from the bottom of the storage formation, m
Δz	infinitesimal vertical distance, m

Greek

α	anisotropy ratio
ϕ	porosity of the storage formation
μ	viscosity of CO_2, kg m^{-1} s^{-1}
$\bar{\mu}$	average viscosity of CO_2, kg m^{-1} s^{-1}
ρ	density of CO_2 as predicted by Altunin's correlations, kg m^{-3}
ρ_P	density of CO_2 as predicted by generalized Pitzer's correlations, kg m^{-3}
ω_a	acentric factor

Acknowledgments

The authors wish to thank the anonymous journal reviewers for their constructive suggestions for improving the quality of this paper. This work was supported by the U.S. Department of Energy. The support is provided to Berkeley Lab through the U.S. Department of Energy Contract No. DE-AC02-05CH11231. The United States Government retains and the publisher, by accepting the article for publication, acknowledges that the United States Government retains a non-exclusive, paid-up, irrevocable, world-wide license to publish or reproduce the published form of this manuscript, or allow others to do so, for United States Government purposes. The views expressed in this article are those of the authors and do not necessarily reflect the views or policies of the United States Department of Energy or the Berkeley Lab.

References

Al-Hussainy, R., Ramey, H.J., Jr., and Crawford, P.B.(1966), The flow of real gases through porous media, Journal of Petroleum Technology, 239, 624-636.

Altunin, V.V. (1975), *Thermophysical Properties of Carbon Dioxide*, Publishing House of Standards, 551 pp., Moscow, Russia (in Russian).

Bachu, S. (2000), Sequestration of CO_2 in geological media: Criteria and approach for site selection in response to climate change, Energy Conversion and Management, 41, 953-970.

Bachu, S. (2008), CO2 storage in geological media: Role, means, status and barriers to deployment, Progress In Energy And Combustion Science, 34(2), 254-273.

Birkholzer, J.T., and Zhou, Q. (2009), Basin-scale hydrogeologic impacts of CO2 storage: Capacity and regulatory implications, International Journal of Greenhouse Gas Control, 3(6), 745-756.

Dentz, M. and Tartakovsky, D.M. (2009), Abrupt-interface solution for carbon dioxide injection into porous media, Transport in Porous Media, 79, 15-27.

Dougherty, D. E., and Babu, D.K. (1984), Flow to a partially penetrating well in a double porosity reservoir, *Water Resources Research*, 20, 1116– 1122.

Ferronato, M., Gambolati, G, Janna, C., Teatini, P. (2010), Geomechanical issues of anthropogenic CO2 sequestration in exploited gas fields, Energy Conversion and Management, 51(10), 1918–1928, doi:10.1016/j.enconman.2010.02.024

Gale, J. (2004), Geological storage of CO_2: What do we know, where are the gaps, and what more needs to be done? Energy, 29 (9-10), 1329-1338.

García, J.E. *Fluid Dynamics of Carbon Dioxide Disposal into Saline Aquifers*, PhD Thesis, University of California at Berkeley, December 2003.

Gunter, W.D., Bachu, S., Law, D.H.-S., Marwaha, V., Drysdale. D.L., McDonald, D.E., McCann, T.J. (1996), Technical and economic feasibility of CO_2 disposal in aquifers within the Alberta sedimentary basin, Canada, Energy Conversion and Management, 37(6-8), 1135-1142.

Hepple, R.P., and Benson, S.M. (2005), Geologic storage of carbon dioxide as a climate change mitigation strategy: Performance requirements and the implications of surface seepage, Environmental Geology, 47, 576-585.

Hildebrand, F. B. (1976), *Advanced Calculus for Applications*, Second Ed., Prentice-Hall, New Jersey.

Holloway, S. (2005), Underground sequestration of carbon dioxide – a viable greenhouse gas mitigation option, Energy, 30, 2318-2333.

Hyder, Z., Butler, J.J., Jr., McElwee, C.D., Liu, W. (1994), Slug tests in partially penetrating wells, *Water Resources Research*, 20(8), 1116-1122.

Leibenzon, L.S. (1929), Gas movement in a porous medium, *Neft. i. Slants. Khoz*., 10, 497-519 (in Russian).

IPCC (Intergovernmental panel on Climate Change) (2005), IPCC Special Report on Carbon Dioxide Capture and Storage, Cambridge University Press, New York, NY.

Mathias, S.A., Hardisty, P.E, Trudell, M.R., and Zimmerman, R.W. (2009a), Approximate solutions for pressure buildup during CO_2 injection in brine aquifers, *Transport in Porous Media*, 79, 265–284.

Mathias, S.A., Hardisty, P.E., Trudell, M.R., and Zimmerman, R.W. (2009b), Screening and selection of sites for CO2 sequestration based on pressure buildup, International Journal of Greenhouse Gas Control 3, 577–585.

Mathias, S.A., de Miguel, G.J.G.M., Thatcher, K.E., and Zimmerman, R.W. (2011), Pressure buildup during CO2 injection into a closed brine aquifer, Transport in Porous Media, doi:10.1007/s11242-011-9776-z.

Muskat, M. (1946), *The flow of homogeneous fluids*, J.E. Edwards, Inc., Ann Arbor, MI.
Muskat, M., and Botset, H.G. (1931), Flow of gases through porous materials, *Physics*, 1, 27-47.

Nordbotten, J.M., Celia, M.A., and Bachu, S. (2005), Injection and storage of CO_2 in deep saline aquifers: analytical solution for CO_2 plume evolution during injection, *Transport in Porous Media*, 58, 339-360.

Oldenburg, C.M. (2006), Geologic carbon sequestration: CO_2 transport in depleted gas reservoirs, in Gas Transport in Porous Media, Ho, C.K. and Webb, S.W. (eds.), pp. 419-426, Springer, London, UK.

Oldenburg, C.M. (2007), Joule-Thomson cooling due to CO_2 injection into natural gas reservoirs, Energy Conversion and Management, 48, 1808-1815.

Oldenburg, C.M. and Doughty, C.A. (2010), Injection, flow and mixing of CO_2 in porous media with residual gas, LBNL-4115E, Transport in Porous Media, published online: DOI: 10.1007/s11242-010-9645-1.

Oruganti, Y., Gupta, A. K., and Bryant, S.L. (2011), Analytical estimation of risk due to pressure buildup during CO_2 injection in deep saline aquifers, Energy Procedia 4, 4140‑4147, doi:10.1016/j.egypro.2011.02.358

Pruess, K. (2005), ECO2N: A TOUGH2 fluid property module for mixtures of water, NaCl, and CO_2, Report LBNL-57952, Lawrence Berkeley National Laboratory, Berkeley, CA.

Pruess, K., Oldenburg, C., and Moridis, G. (1999), TOUGH2 User's Guide, Version 2.0, Report LBNL-43134, Lawrence Berkeley National Laboratory, Berkeley, CA.

Saripalli, P., and McGrail, P. (2002), Semi-analytical approaches to modeling deep well injection of CO_2 for geological sequestration, Energy Conversion and Management, 43(2), 185–198.

Smith, J.M. and Van Ness, H.C. (1981), *Introduction to Chemical Engineering Thermodynamics*, 3rd edition (9th printing), International Student Edition, McGraw-Hill, New Delhi, India.

Tartakovsky, D.M. (2000), Real gas flow through heterogeneous porous media: theoretical aspects of upscaling, *Stochastic Environmental Research and Risk Assessment*, 14, 109-122.

Vilarrrasa, V., Bolster, D., Olivella, S., and Carrera, J. (2010a), Coupled hydromechanical modeling of CO_2 sequestration in deep saline aquifers, International Journal of Greenhouse Gas Control, 4(6), 910-919.

Vilarrasa, V., Bolster, D., Dentz, M., Olivella, S., and Carrera, J. (2010b), Effects of CO_2 compressibility on CO_2 storage in deep saline aquifers, *Transport In Porous Media*, DOI: 10.1007/s11242-010-9582-z.

Yang, S.-Y., Yeh, H.-D., Chiu, P.Y. (2006), A closed form solution for constant flux pumping in a well under partial penetration condition, Water Resources Research, 42, W05502, doi:10.1029/2004WR003889.

Yeh, H.-D., Yang, S.-Y., Peng, H.Y. (2003), A new closed-form solution for a radial two-layer drawdown equation for groundwater under constant flux pumping in a finite-radius well, Adv. Water Resour., 26(7), 747-757.

Yeh, H.-D., Chen, Y.-J., and Yang, S.-Y. (2008), Semi-analytical solution for a slug test in partially penetrating wells including the effect of finite-thickness skin, *Hydrological Processes*, 22, 3741-3748.

Zeidouni, M., Pooladi-Darvish, M., and Keith, D.W. (2011), Analytical Models for Determining Pressure Change in an Overlying Aquifer due to Leakage, Energy Procedia 4, 3833‑3840, doi:10.1016/j.egypro.2011.02.319

Zhou, Q., Birkholzer, J., Tsang, C.-F. (2009), A semi-analytical solution for large-scale injectioninduced pressure perturbation and leakage in a laterally bounded aquifer-aquitard system, *Transport in Porous Media* 78(1), 127-148.

Zhou, Q., and Birkholzer, J.T. (2011), On scale and magnitude of pressure build-up induced by large-scale geologic storage of CO_2, Greenhouse Gas Sci Technol, 1, 11–20, doi: 10.1002/ghg3

Figure Captions

Figure 1. Schematic diagram showing the conceptual model used for developing the analytical solution for migration of CO_2 after being injected into a natural gas storage formation. Note that the transport processes within the injection borehole has not been included in the conceptual model

Figure 2. Reduced volume (V_r) of CO_2 as a function of pressure at different temperatures. The horizontal dotted line represents $V_r = 2$. The reduced volumes have been calculated using Altunin's correlations (1975), and have been obtained from the CO2TAB file distributed with the TOUGH2/ECO2N software (Pruess, 2005)

Figure 3a. The actual difference in densities computed using Altunin's correlations and generalized Pitzer's correlations as a function of pressure at different temperatures

Figure 3b. The actual and fitted difference in densities computed using Altunin's correlations and generalized Pitzer's correlations at different temperatures as a function of pressure up to the turnover pressure

Figure 4. Comparison of predicted pressure buildup by the analytical approach and numerical simuations. Pressure is shown as a function of time when formation temperature is 55^{o}C, formation permeability is 1×10^{-14} m^2, and anisotropy ratio is unity

Figure 5. Predicted pressure buildup as a function of radial distance with different anisotropy ratios, when formation temperature is 55^{o}C and formation permeability is 1×10^{-14} m^2

Figure 6. Predicted pressure buildup as a function of time with different anisotropy ratios, when formation temperature is 55^{o}C and formation permeability is 1×10^{-14} m^2

Figure 7a. Predicted pressure buildup as a function of radial distance at 1 year with different formation horizontal (radial) permeabilities, when formation temperature is 55^{o}C and anisotropy ratio is unity

Figure 7b~~a~~. Predicted pressure buildup as a function of radial distance at 30 years with different formation horizontal (radial) permeabilities, when formation temperature is 55^{o}C and anisotropy ratio is unity

Figure 8a. Predicted pressure buildup as a function of time at r = 10.0~~10~~ m with different formation horizontal (radial) permeabilities, when formation temperature is 55^{o}C and anisotropy ratio is unity

Figure 8b. Predicted pressure buildup as a function of time at r = 0.1~~0.1~~ m with different formation horizontal (radial) permeabilities, when formation temperature is 55^{o}C and anisotropy ratio is unity

Figure 9. The closed-contour integration of $\hat{\theta}_D$ for the Bromwich integral

Table Captions

Table 1. The coefficients a_n as discussed in Equation 4. These parameters provide the correction factors needed to account for difference in density values predicted by the generalized Pitzer's correlations and those predicted by Altunin's correlations. The rightmost column provides the range of pressure over which these relationships are valid. The upper limit of the pressure range is the P_{to}

Table 2. Geometrical and physical properties of the storage formation, initial and boundary conditions, and injection rate used in the computations.

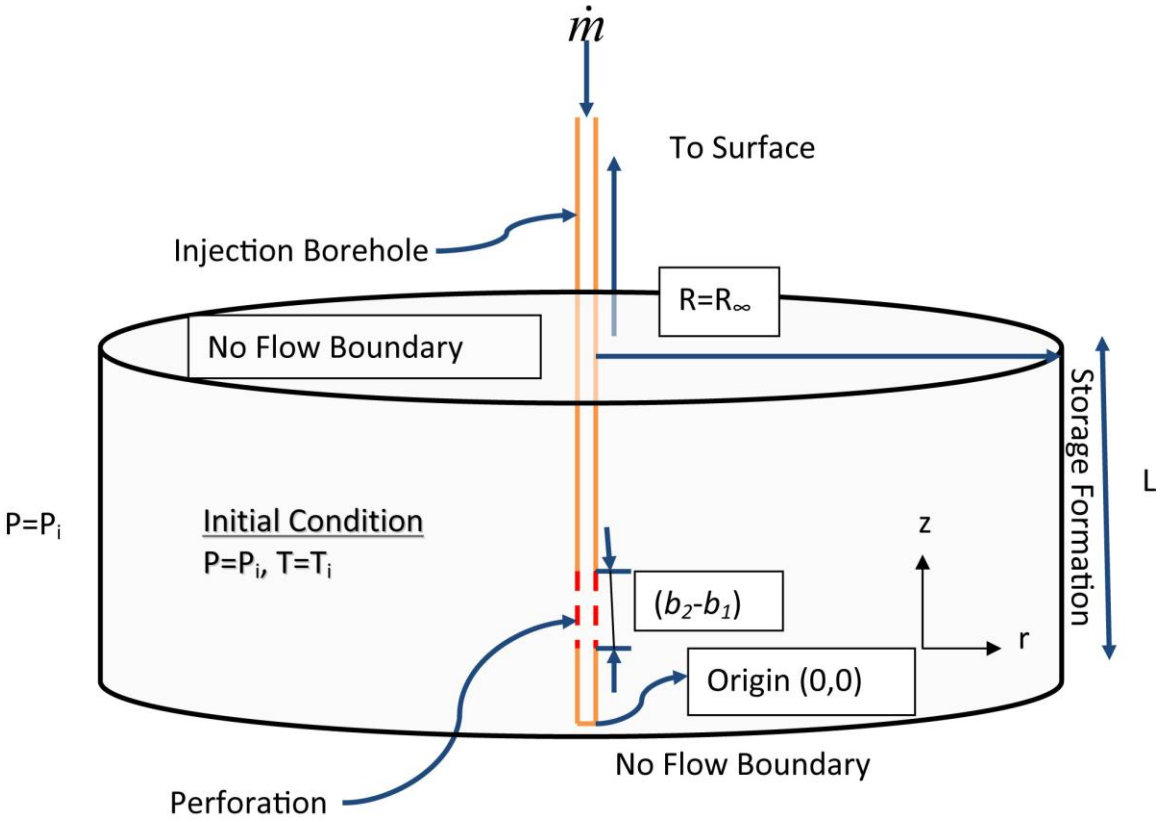
$\dot{m}$
To Surface
Injection Borehole
R=R∞
No Flow Boundary
Storage Formation
L
P=Pi
Initial Condition
P=Pi, T=Ti
z
r
(b2-b1)
Origin (0,0)
No Flow Boundary
Perforation

Figure 1.

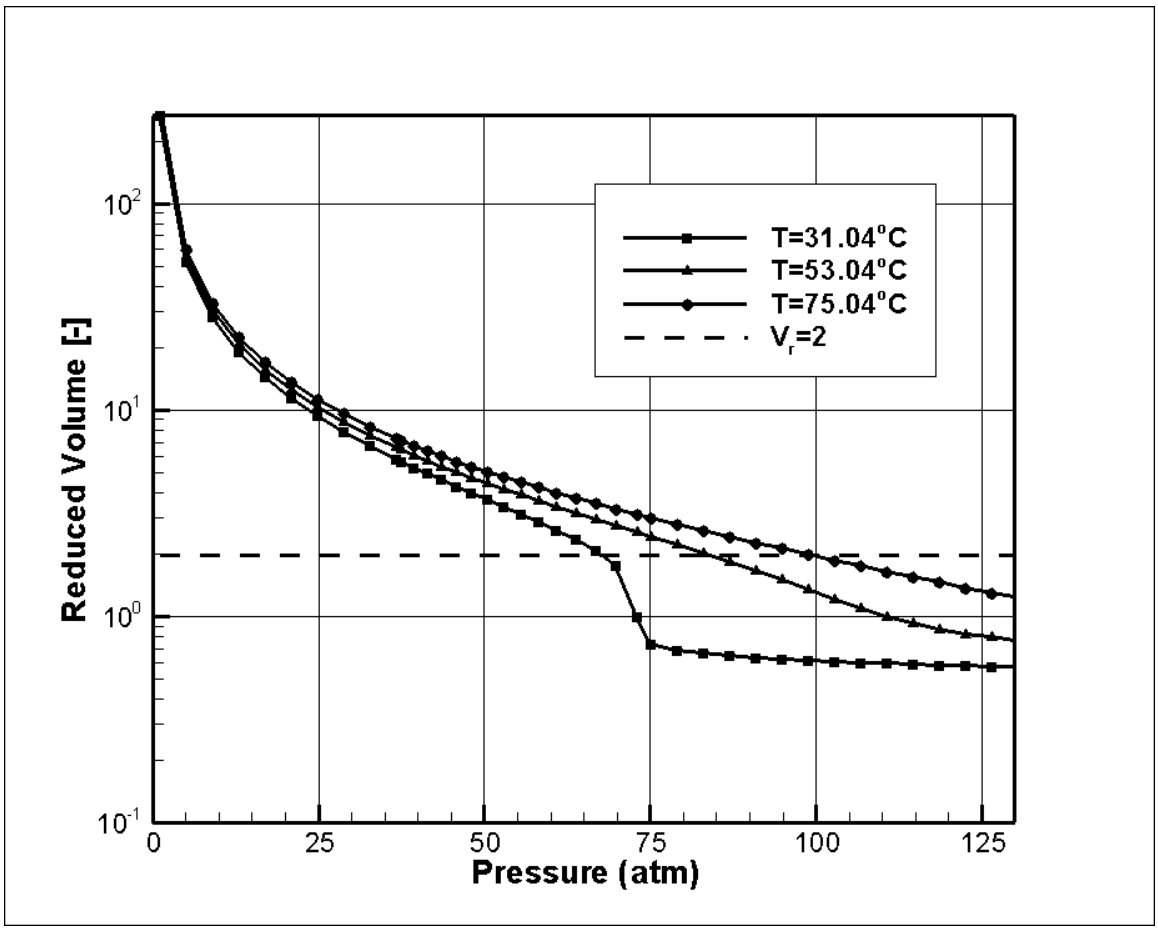
Reduced Volume [-]
Pressure (atm)
T=31.04°C
T=53.04°C
T=75.04°C
V_r=2
10^2
10^1
10^0
10^-1
0
25
50
75
100
125
Figure 2.

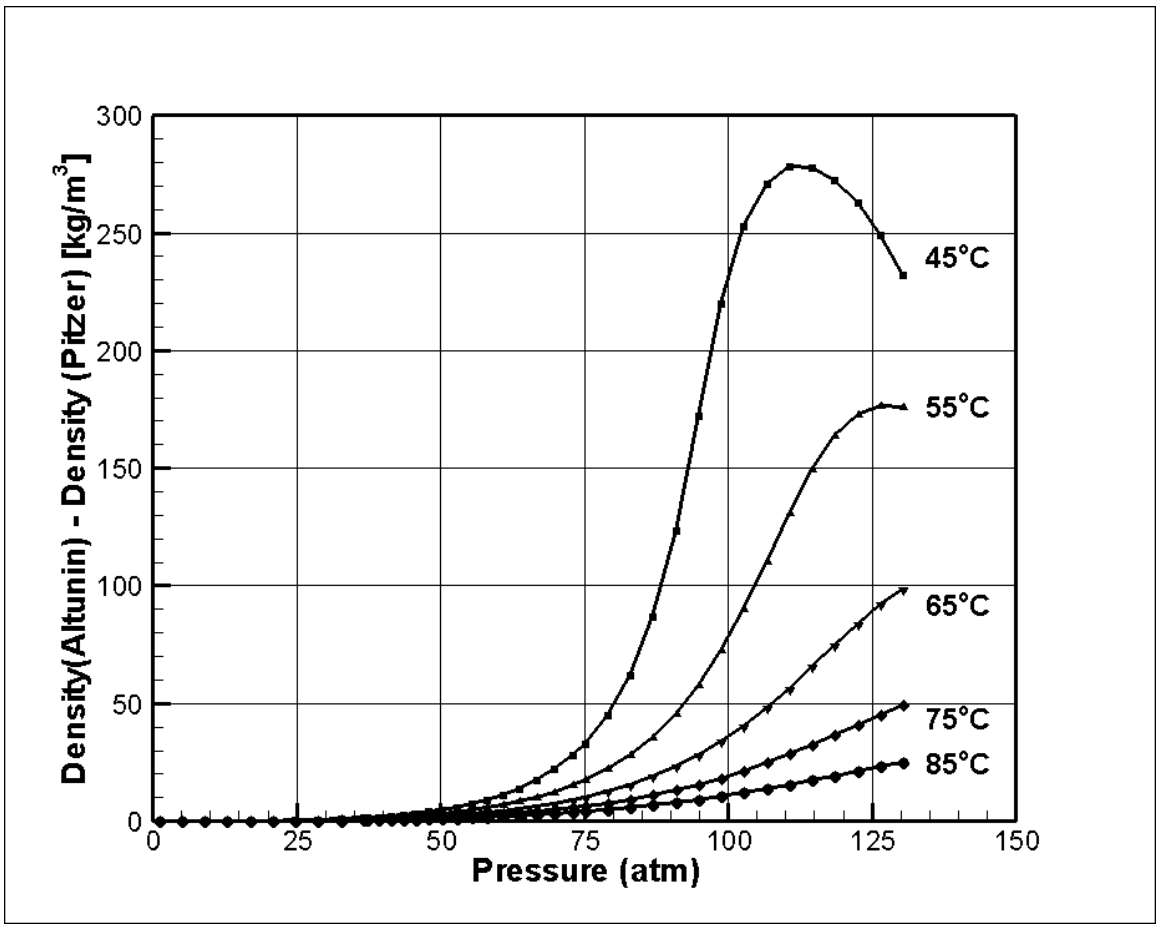
Density(Altunin) - Density (Pitzer) [kg/m3]
Pressure (atm)
45°C
55°C
65°C
75°C
85°C
0
50
100
150
200
250
300
0
25
50
75
100
125
150
Figure 3a.

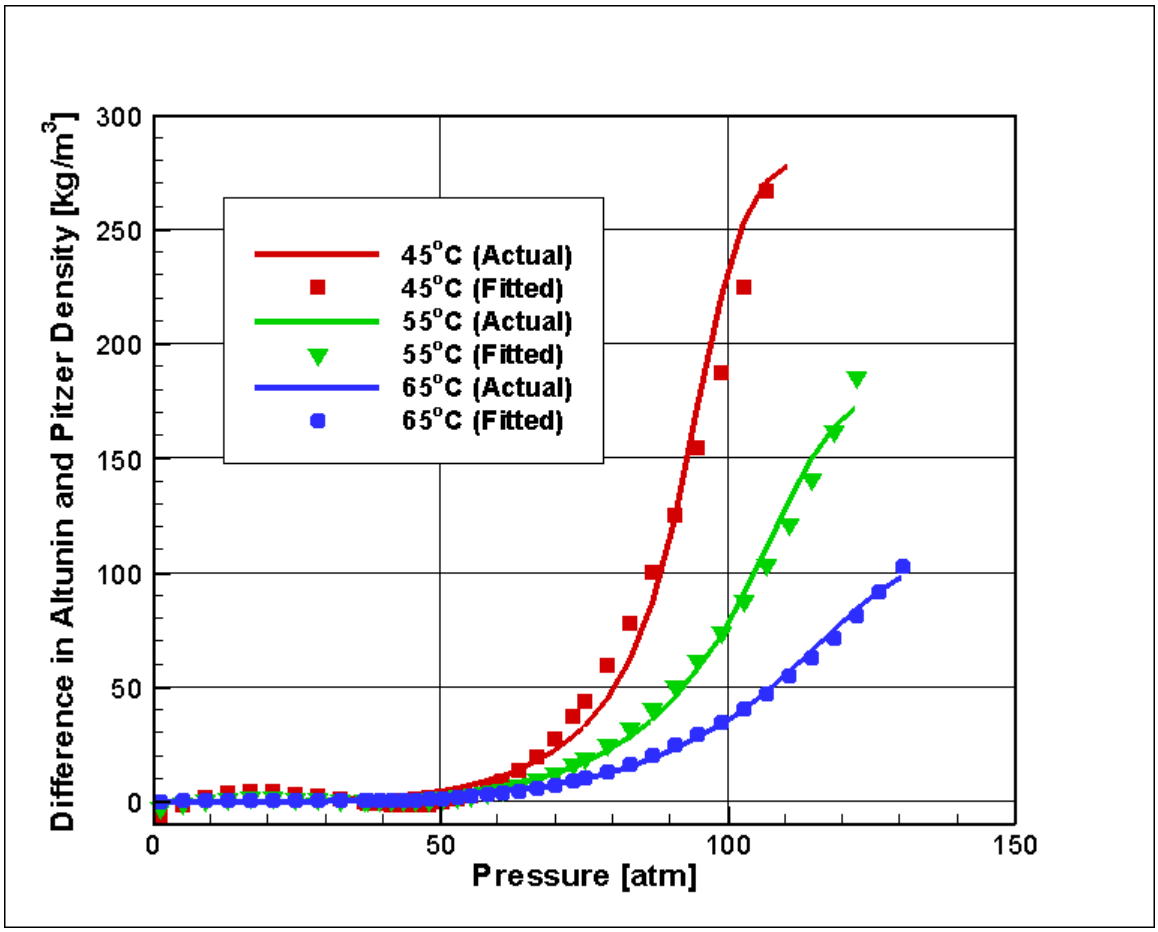
Difference in Altunin and Pitzer Density [kg/m3]
Pressure [atm]
45°C (Actual)
45°C (Fitted)
55°C (Actual)
55°C (Fitted)
65°C (Actual)
65°C (Fitted)
0
50
100
150
200
250
300
Figure 3b.

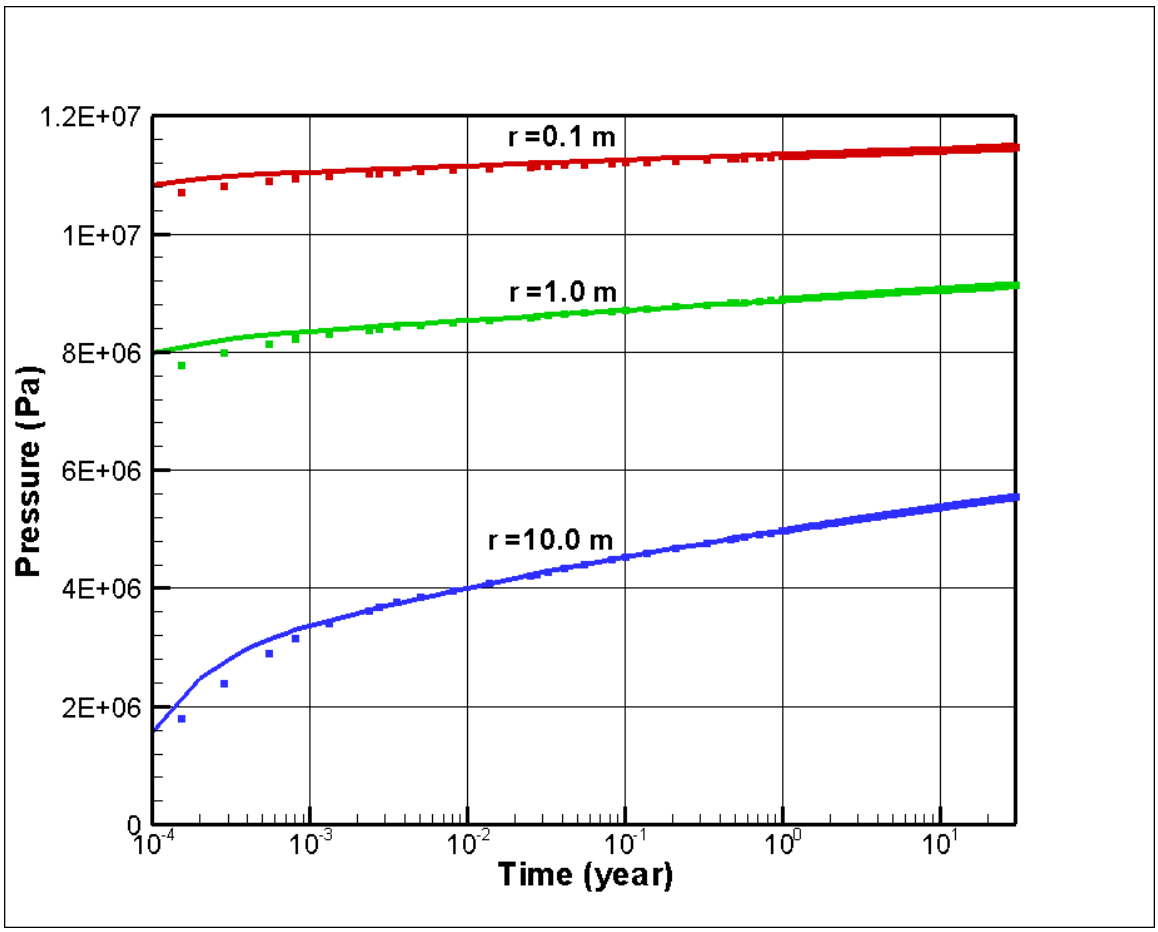
1.2E+07
1E+07
8E+06
6E+06
4E+06
2E+06
0
Pressure (Pa)
r =0.1 m
r =1.0 m
r =10.0 m
10-4
10-3
10-2
10-1
100
101
Time (year)
Figure 4.

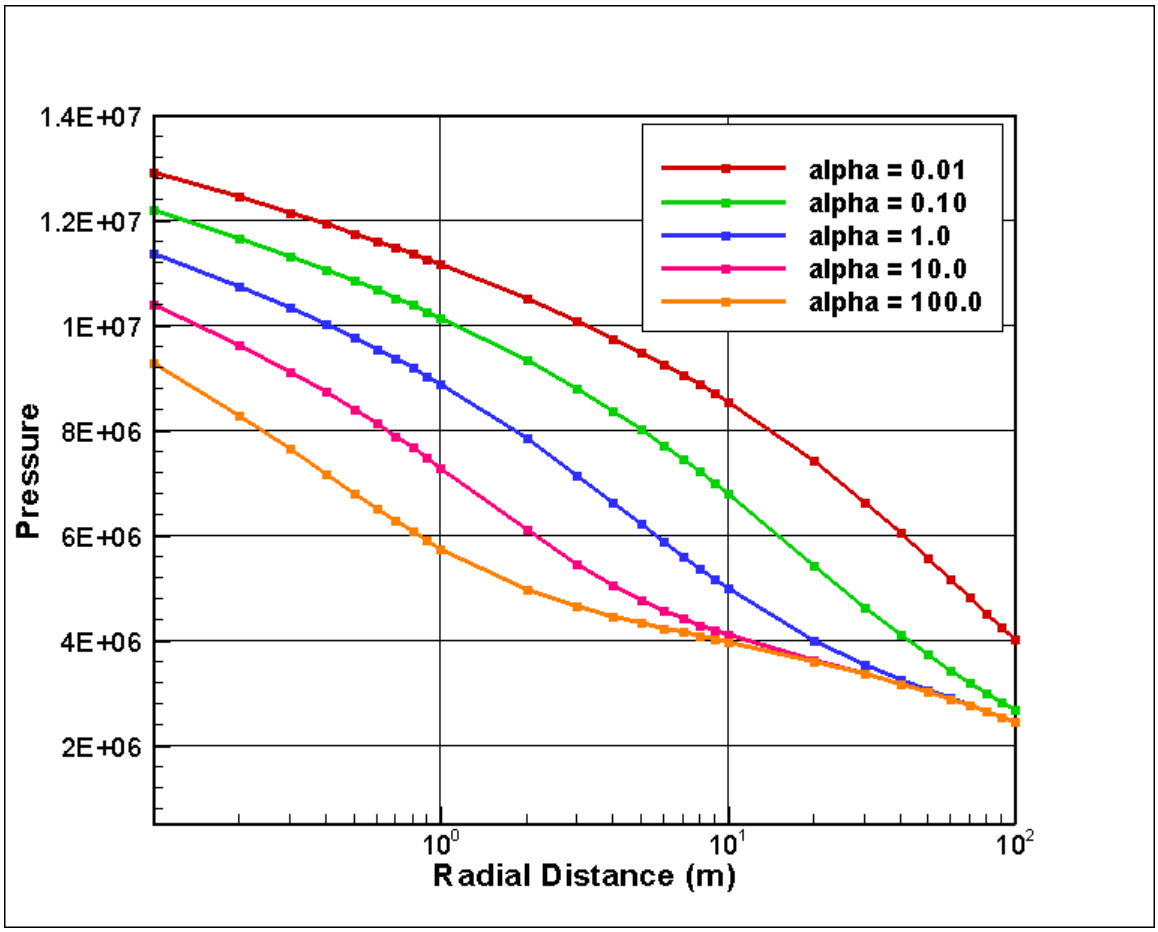
1.4E+07
1.2E+07
1E+07
8E+06
6E+06
4E+06
2E+06
Pressure
10^0
10^1
10^2
Radial Distance (m)
alpha = 0.01
alpha = 0.10
alpha = 1.0
alpha = 10.0
alpha = 100.0
Figure 5.

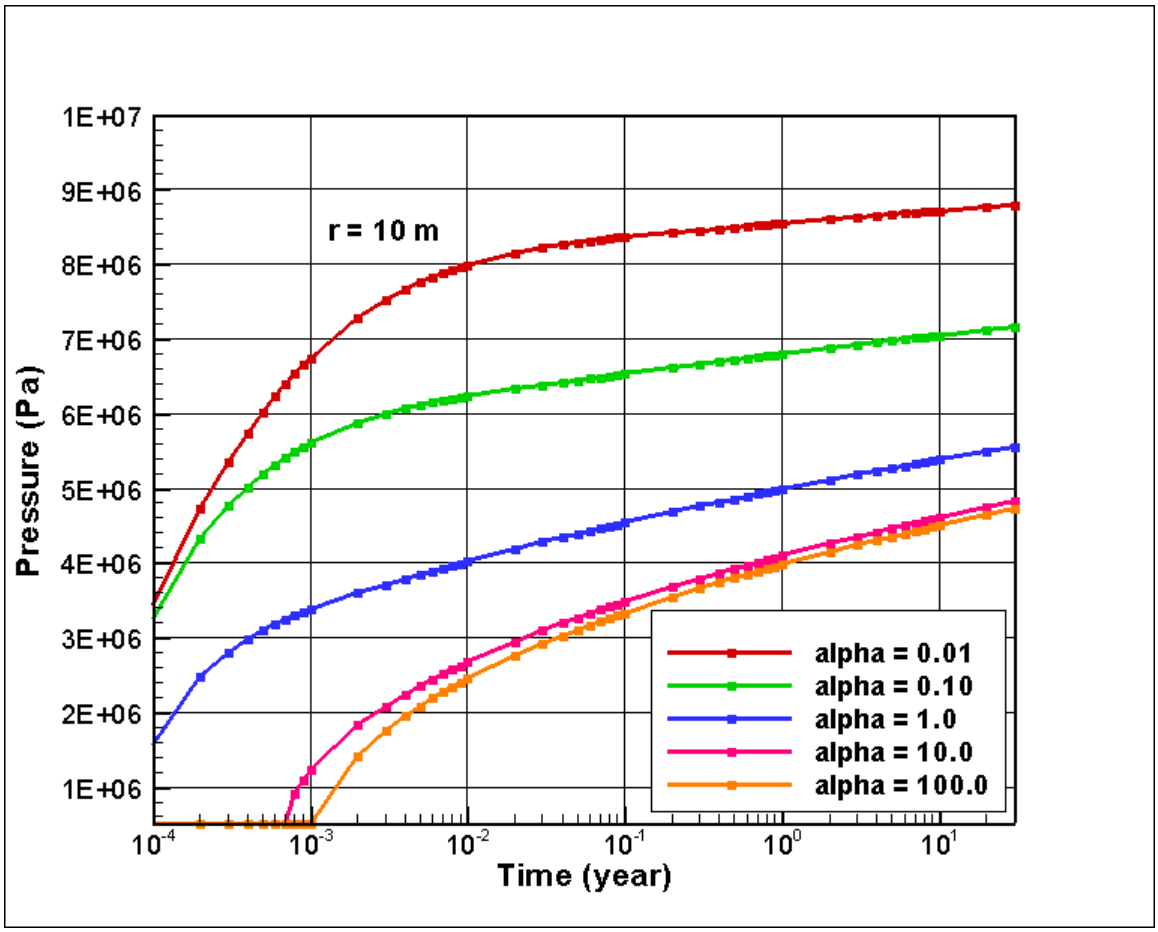
r = 10 m
Pressure (Pa)
Time (year)
1E+07
9E+06
8E+06
7E+06
6E+06
5E+06
4E+06
3E+06
2E+06
1E+06
10^-4
10^-3
10^-2
10^-1
10^0
10^1
alpha = 0.01
alpha = 0.10
alpha = 1.0
alpha = 10.0
alpha = 100.0
Figure 6.

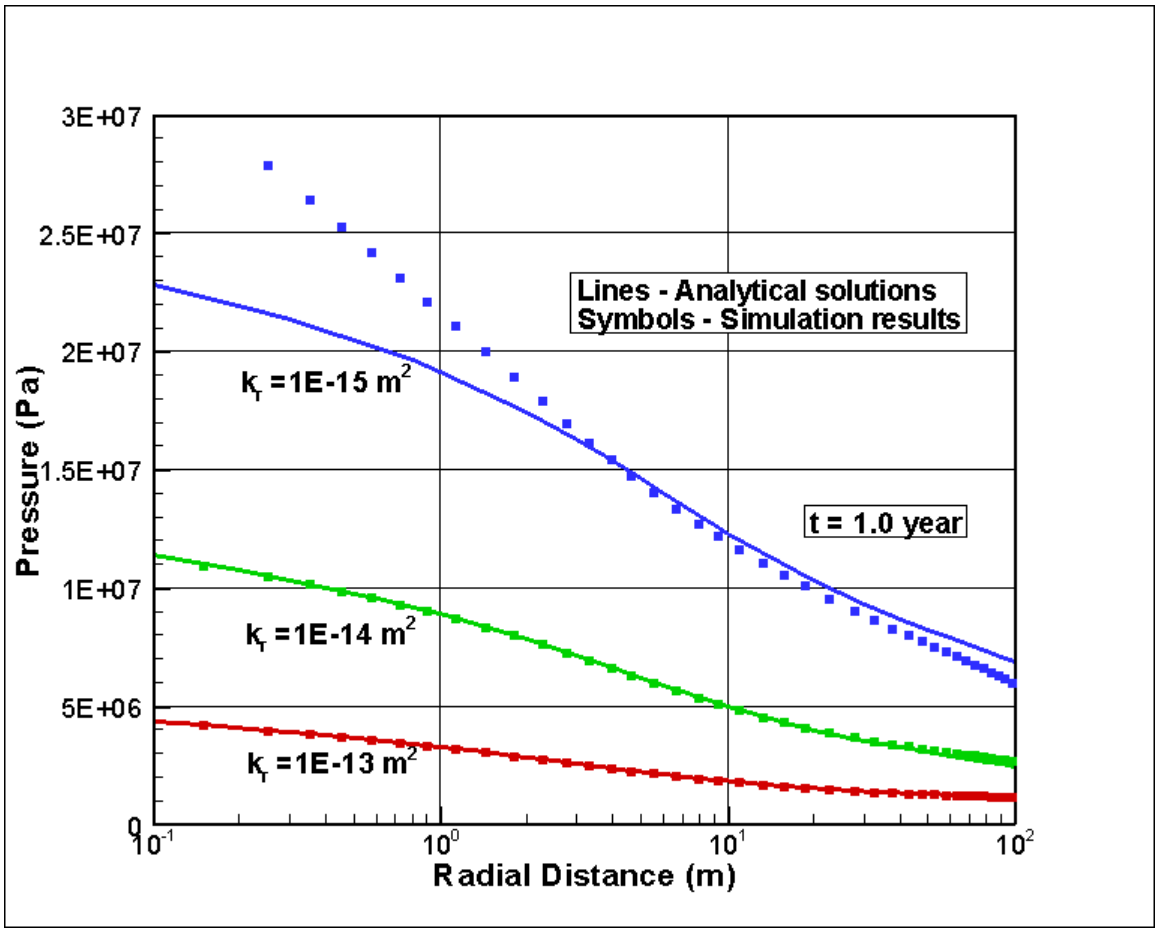
3E+07
2.5E+07
2E+07
1.5E+07
1E+07
5E+06
0
Pressure (Pa)
Lines - Analytical solutions
Symbols - Simulation results
k_r =1E-15 m^2
k_r =1E-14 m^2
k_r =1E-13 m^2
t = 1.0 year
10^-1
10^0
10^1
10^2
Radial Distance (m)
Figure 7a.

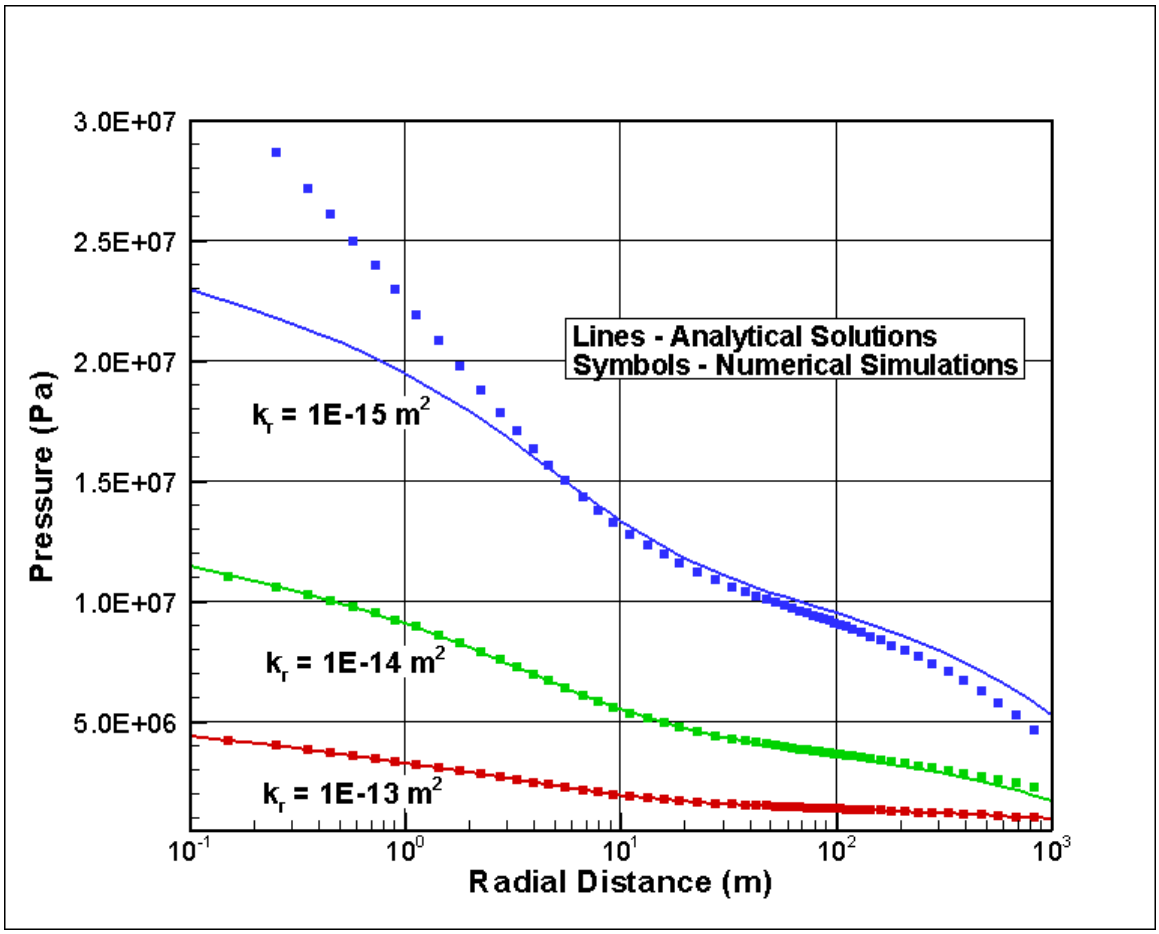
3.0E+07
2.5E+07
2.0E+07
1.5E+07
1.0E+07
5.0E+06
Pressure (Pa)
Lines - Analytical Solutions
Symbols - Numerical Simulations
k_r = 1E-15 m^2
k_r = 1E-14 m^2
k_r = 1E-13 m^2
10^-1
10^0
10^1
10^2
10^3
Radial Distance (m)
Figure 7b.

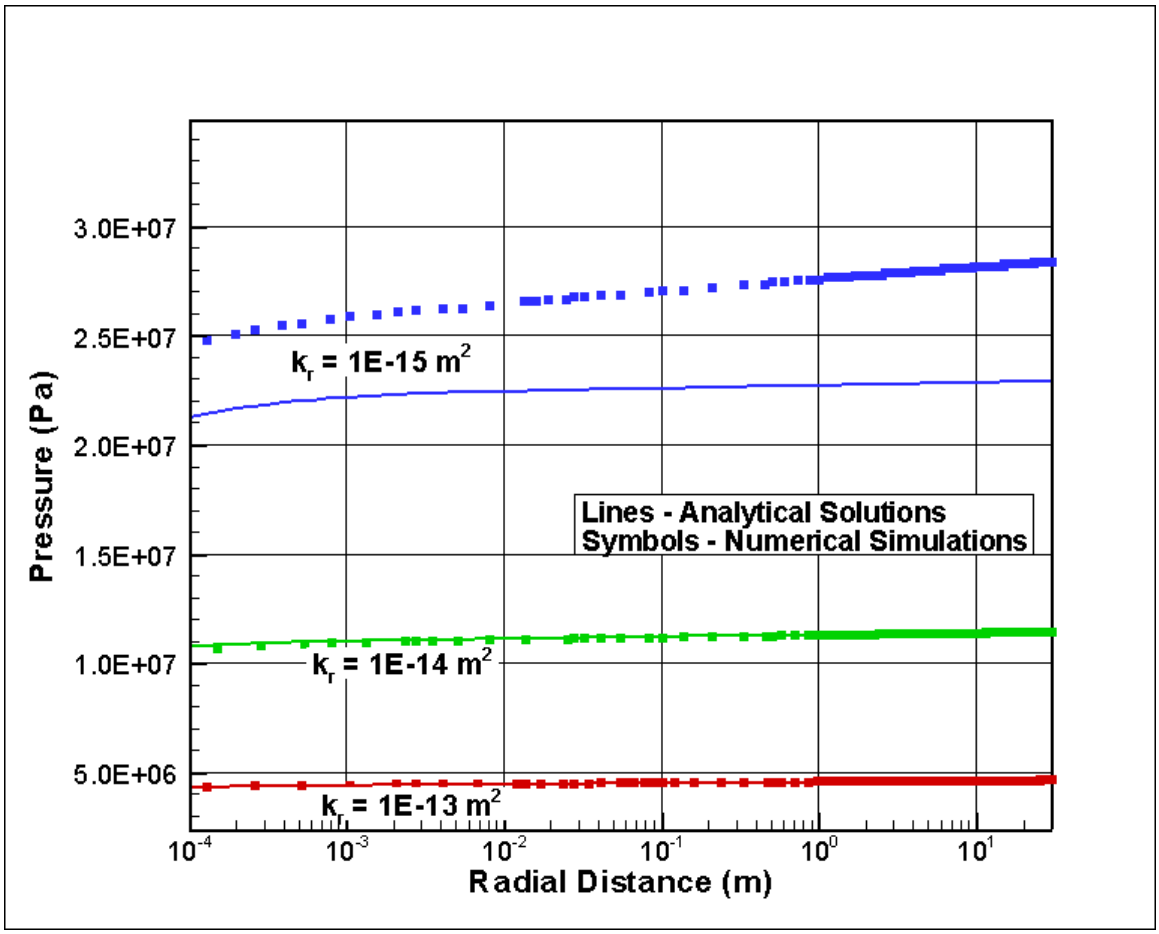
3.0E+07
2.5E+07
2.0E+07
1.5E+07
1.0E+07
5.0E+06
Pressure (Pa)
k_r = 1E-15 m^2
k_r = 1E-14 m^2
k_r = 1E-13 m^2
Lines - Analytical Solutions
Symbols - Numerical Simulations
10^{-4}
10^{-3}
10^{-2}
10^{-1}
10^{0}
10^{1}
Radial Distance (m)
Figure 8a.

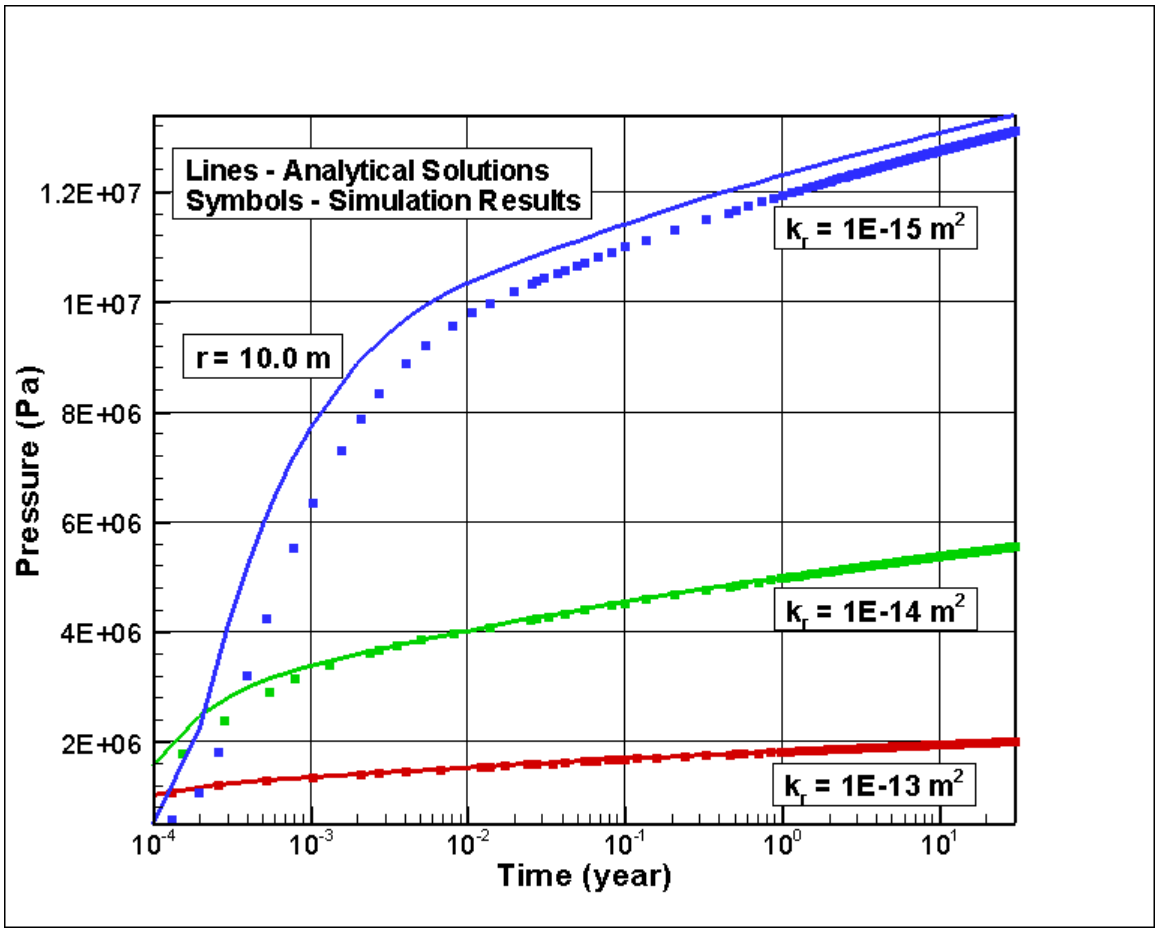
Lines - Analytical Solutions
Symbols - Simulation Results
r = 10.0 m
k_r = 1E-15 m^2
k_r = 1E-14 m^2
k_r = 1E-13 m^2
Pressure (Pa)
1.2E+07
1E+07
8E+06
6E+06
4E+06
2E+06
10^{-4}
10^{-3}
10^{-2}
10^{-1}
10^{0}
10^{1}
Time (year)
Figure 8b.

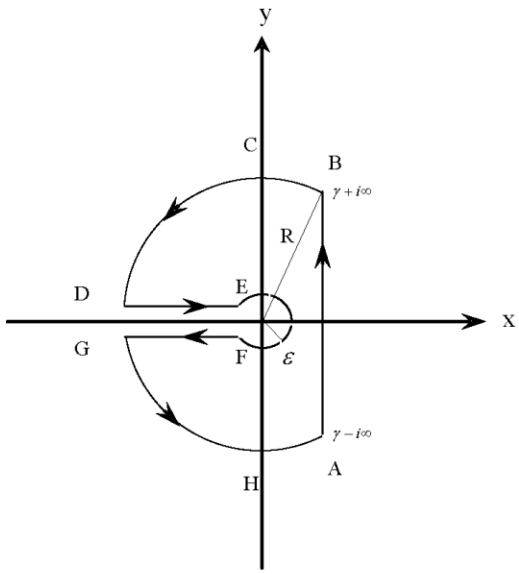

Figure 9.

Table 1.

No.	Temperature (T) [^{o}C]	a_0 [kg m^{-3}]	a_1 [kg m^{-3} atm^{-1}]	a_2 [kg m^{-3} atm^{-2}]	a_3 [kg m^{-3} atm^{-3}]	Range of Pressure [atm]
1.	45	-0.0574	0.0660	-0.0083	2.7×10^{-4}	1-106
2.	55	-0.0243	0.0280	-0.0035	1.1×10^{-4}	1-126
3.	65	-0.0209	0.0234	-0.0023	6.1×10^{-5}	1-138

Table 2.

Parameter	Value
Injection rate	250,000 tons/year
Injection period	30 years
Formation thickness	100 m
Top of formation	55 m
Bottom of formation	45 m
Perforation thickness	10 m
Injection well radius	0.1 m
Initial formation pressure	5×10^{5} Pa
Formation temperature	55^{o}C
Formation porosity	0.1
Formation permeability	1×10^{-14} m^{2}